Self-Assembly of CdTe Nanocrystals into Free-Floating Sheets

Zhiyong Tang, *et al.*

Science **314**, 274 (2006);
DOI: 10.1126/science.1128045

and extent of *CAN*-gene mutations in breast and colorectal cancers, whether these genes are mutated in other tumor types, and whether germline variants in *CAN* genes are associated with cancer predisposition. For immunology, the finding that tumors contain an average of ~90 different amino acid substitutions not present in any normal cell can provide novel approaches to engender antitumor immunity. For epidemiology, the remarkable difference in mutation spectra of breast and colorectal cancers suggests the existence of organ-specific carcinogens. For cancer biology, it is clear that no current animal or in vitro model of cancer recapitulates the genetic landscape of an actual human tumor. Understanding and capturing this landscape and its heterogeneity may provide models that more successfully mimic the human disease. For epigenetics, it is possible that a subset of *CAN* genes can also be dysregulated in tumors through changes in chromatin or DNA methylation rather than through mutation. For diagnostics, the *CAN* genes define a relatively small subset of genes that could prove useful as markers for neoplasia. Finally, some of these genes, particularly those on the cell surface or those with enzymatic activity, may prove to be good targets for therapeutic development.

References and Notes

1. B. Vogelstein, K. W. Kinzler, *Nat. Med.* **10**, 789 (2004).
2. P. A. Futreal *et al.*, *Nat. Rev. Cancer* **4**, 177 (2004).
3. A. Bardelli, V. E. Velculescu, *Curr. Opin. Genet. Dev.* **15**, 5 (2005).
4. B. Vogelstein, K. W. Kinzler, *The Genetic Basis of Human Cancer* (McGraw-Hill, Toronto, 2002).
5. D. M. Parkin, F. Bray, J. Ferlay, P. Pisani, *CA Cancer J. Clin.* **55**, 74 (2005).
6. CCDS Database (www.ncbi.nlm.nih.gov/CCDS).
7. See supporting material on *Science* Online.
8. B. Ewing, P. Green, *Genome Res.* **8**, 186 (1998).
9. C. Lengauer, K. W. Kinzler, B. Vogelstein, *Nature* **396**, 643 (1998).
10. L. A. Loeb, *Cancer Res.* **61**, 3230 (2001).
11. C. Greenman, R. Wooster, P. A. Futreal, M. R. Stratton, D. F. Easton, *Genetics* **173**, 2187 (2006).
12. S. E. Kern, J. M. Winter, *Cancer Biol. Ther.* **5**, 349 (2006).
13. T. L. Wang *et al.*, *Proc. Natl. Acad. Sci. U.S.A.* **99**, 3076 (2002).
14. D. Shen *et al.*, in preparation.
15. P. Stephens *et al.*, *Nat. Genet.* **37**, 590 (2005).
16. H. Strohmaier *et al.*, *Nature* **413**, 316 (2001).
17. A. Bardelli *et al.*, *Science* **300**, 949 (2003).
18. Z. Wang *et al.*, *Cancer Res.* **64**, 2998 (2004).
19. G. J. Riggins *et al.*, *Nat. Genet.* **13**, 347 (1996).
20. K. Eppert *et al.*, *Cell* **86**, 543 (1996).
21. J.-L. Ku *et al.*, *Cancer Lett.* 10.1016/j.canlet.2006.05.008 (2006).
22. A. Duval *et al.*, *Cancer Res.* **59**, 4213 (1999).
23. S. Markowitz *et al.*, *Science* **268**, 1336 (1995).
24. C. A. Landis *et al.*, *Nature* **340**, 692 (1989).
25. B. Padmanabhan *et al.*, *Mol. Cell* **21**, 689 (2006).
26. O. Bluteau *et al.*, *Nat. Genet.* **32**, 312 (2002).
27. K. Salassidis *et al.*, *Cancer Res.* **60**, 2786 (2000).
28. Y. Arai *et al.*, *Blood* **89**, 3936 (1997).
29. K. W. Kinzler *et al.*, *Science* **236**, 70 (1987).
30. H. Varmus, *Science* **312**, 1162 (2006).
31. X. X. Tang, G. M. Brodeur, B. G. Campling, N. Ikegaki, *Clin. Cancer Res.* **5**, 455 (1999).
32. M. Ruault, M. E. Brun, M. Ventura, G. Roizes, A. De Sario, *Gene* **284**, 73 (2002).
33. M. Tanaka *et al.*, *Cancer Res.* **55**, 3228 (1995).
34. A. Sasaki, Y. Masuda, Y. Ohta, K. Ikeda, K. Watanabe, *J. Biol. Chem.* **276**, 17871 (2001).
35. M. Sato *et al.*, *Genes Chromosomes Cancer* **44**, 405 (2005).
36. Y. Onishi, K. Tsukada, J. Yokota, A. Raz, *Clin. Exp. Metastasis* **20**, 51 (2003).
37. M. Hollstein, D. Sidransky, B. Vogelstein, C. C. Harris, *Science* **253**, 49 (1991).
38. J. L. Bos *et al.*, *Nature* **327**, 293 (1987).
39. R. Brent, *Cell* **100**, 169 (2000).
40. T. Ideker *et al.*, *Science* **292**, 929 (2001).
41. S. L. Ooi *et al.*, *Trends Genet.* **22**, 56 (2006).
42. T. Soussi, G. Lozano, *Biochem. Biophys. Res. Commun.* **331**, 834 (2005).
43. M. Olivier, S. P. Hussain, C. Caron de Fromentel, P. Hainaut, C. C. Harris, *IARC Sci. Publ. 157*, 247 (2004).
44. J. F. Costello *et al.*, *Nat. Genet.* **24**, 132 (2000).
45. A. H. Owens, D. S. Coffey, S. B. Baylin, Eds., *Tumor Cell Heterogeneity* (Academic Press, New York, 1982), pp. 441–460.
46. K. D. Pruitt, T. Tatusova, D. R. Maglott, *Nucleic Acids Res.* **33**, D501 (2005).
47. The Cancer Genome Atlas (http://cancergenome.nih.gov/index.asp).
48. Y. H. Rogers, J. C. Venter, *Nature* **437**, 326 (2005).

49. We thank J. Lutterbaugh, E. Lawrence, and L. Beard for assistance with cell culture and DNA preparation; E. Suh, D. Smith, K. Makowski, and the Agencourt sequencing team for assistance with automated sequencing; S. Kern for helpful comments on the manuscript; and R. J. Vogelstein and J. T. Vogelstein for assistance with statistical analyses. Supported by the Virginia and D. K. Ludwig Fund for Cancer Research; NIH grants CA 121113, CA 43460, CA 57345, CA 62924, GM 07309, RR 017698, P30-CA43703, and CA109274; NCI Division of Cancer Prevention contract HHSN261200433002C; Department of Defense grant DAMD17-03-1-0241; and the Pew Charitable Trusts, the Palmetto Health Foundation, the Maryland Cigarette Restitution Fund, the State of Ohio Biomedical Research and Technology Transfer Commission, the Clayton Fund, the Blaustein Foundation, the National Colorectal Cancer Research Alliance, the Avon Foundation, the Flight Attendant Medical Research Institute, and the V Foundation for Cancer Research.

Supporting Online Material

www.sciencemag.org/cgi/content/full/1133427/DC1
Materials and Methods
Figs. S1 and S2
Tables S1 to S5
References

3 August 2006; accepted 30 August 2006
Published online 7 September 2006;
10.1126/science.1133427
Include this information when citing this paper.

REPORTS

Self-Assembly of CdTe Nanocrystals into Free-Floating Sheets

Zhiyong Tang,[1]* Zhenli Zhang,[1] Ying Wang,[2] Sharon C. Glotzer,[1,2]† Nicholas A. Kotov[1,2,3]†

In their physical dimensions, surface chemistry, and degree of anisotropic interactions in solution, CdTe nanoparticles are similar to proteins. We experimentally observed their spontaneous, template-free organization into free-floating particulate sheets, which resemble the assembly of surface layer (S-layer) proteins. Computer simulation and concurrent experiments demonstrated that the dipole moment, small positive charge, and directional hydrophobic attraction are the driving forces for the self-organization process. The data presented here highlight the analogy of the solution behavior of the two vastly different classes of chemical structures.

Understanding the ability of nanoparticles (NPs) to self-assemble will influence both the fundamental picture of the properties of matter on the nanoscale and the practical realization of bottom-up fabrication technologies (*1*–*3*). Self-organization processes in solution have been well established for proteins and other biomacromolecules (*4*–*6*), which have physical dimensions of several nanometers, i.e., the same scale as that of many inorganic nanocolloids. Recent studies demonstrate nanoparticle self-organization into one-dimensional (1D) structures driven by anisotropic dipolar interparticle forces (*7*–*9*). Highly uniform nanocolloids, with presumably isotropic interactions, can form 3D arrays or crystals (*10*–*14*). Two-dimensional arrays of NPs produced at two-phase interfaces—such as gas-solid (*10*), liquid-solid (*15*), gas-liquid (*16*), or liquid-liquid (*17*)—where the interfaces act as a template, are well known. We report that the combination of the electrostatic interaction and anisotropic hydrophobic attraction between NPs with tetrahedral shape result in the spontaneous formation of 2D free-floating sheets. The sheets display considerable mechanical robustness and retain size-quantized properties of the semiconductor NP with characteristic luminescence. Notably, they do not require any interface that may give dimension-restrictive cues

[1]Department of Chemical Engineering, University of Michigan, Ann Arbor, MI 48109–2136, USA. [2]Department of Materials Science and Engineering, University of Michigan, Ann Arbor, MI 48109–2136, USA. [3]Department of Biomedical Engineering, University of Michigan, Ann Arbor, MI 48109–2136, USA.

*Present address: National Center for Nanoscience and Technology, Beijing 100080, China.
†To whom correspondence should be addressed. E-mail: kotov@umich.edu (N.A.K.); sglotzer@umich.edu (S.C.G.)

and form entirely due to specific NP-NP interactions, which changes the paradigm of self-organization processes for NPs.

2-(Dimethylamino)ethanethiol (DMAET)–stabilized CdTe NPs with positive charges were synthesized by the Rogach-Weller method (*18*, *19*). Transmission electron microscopy (TEM) (Fig. 1A) and tapping-mode atomic force microscopy (AFM) images (Fig. 1B) indicate the formation of objects that can be characterized as free-floating sheets formed by a 2D network of assembled NPs (Fig. 1C). In both TEM and AFM images, these sheets appear as flat, semifolded, and even wrinkled platelets. The semifolded structures demonstrate that the 2D NP sheets form in solution rather than on the substrate during drying. Using TEM, we estimate that more than 99% of the NPs assembled into sheets. We found similar sheets for CdSe NPs when we used the same stabilizer, which indicates the potential generality of the phenomenon (fig. S3).

The sheets possess some physical integrity, and some pieces as large as 50 μm by 30 μm (Fig. 1A) remain after gentle stirring and drying. The average AFM thickness of the NP sheets is 3.4 ± 0.2 nm (50 measurements). Because our DMAET-stabilized CdTe nanocrystals are 3.4 nm in diameter as determined by TEM, we conclude that the sheets are monolayers. A total height of 6.8 nm is found for smaller pieces spread atop larger ones and corresponds to the height of NP bilayers (Fig. 1B).

The NP sheets in solution have easily detectable photoluminescence (PL) with a quantum yield of 2.1%, which is considerably lower than the 30% quantum yield of the unassembled CdTe. The assembly also caused the PL peak to be red-shifted from 557 to 564 nm, i.e., by 27 meV (Fig. 2A). These observations are consistent with PL quenching due to excitation transfer in the closely spaced NP system also resulting in the preferential emission from larger NPs (*20*, *21*). Nevertheless, the optical activity is sufficiently high to obtain confocal microscopy images under ambient conditions (Fig. 2, C and D). The confocal images correlate well with the TEM and AFM micrographs. The green-yellow emission of the films is the same over the entire sheet regardless of size, and the corresponding PL image matches the optical image (Fig. 2, B and C), which reflects the equal degree of quantization of the NPs that form the free-floating film. In this size regime, the emission color of CdTe is extremely sensitive to changes in particle diameter. Thus, the particles retain the individuality of their semiconducting cores. The same conclusion can be reached with CdTe NPs of different diameters (from 2.4 to 5.0 nm) and with different PL wavelengths (Fig. 2D). Confocal images also indicate that the interparticle forces driving sheet formation do not involve recrystallization of the CdTe atomic structure as observed in the self-assembly of CdTe nanowires (*7*); otherwise, color variations would have been observed. Some intensity variations along the sheet surface reflect the presence of films with double thicknesses due to additional pieces picked up from the solution (Fig. 1, A and B).

What is the mechanism underlying the formation of free-floating NP sheets rather than traditional 3D agglomeration and precipitation? One hypothesis, that sheets form on the vessel walls, has been excluded after multiple blank experiments based on a variety of techniques (see supporting online material). The results of confocal optical microscopy (fig. S1), light-scattering data (fig. S2, A to E), and TEM of the intermediate state (fig. S2F) are consistent with this conclusion. Semiconductor nanocolloids with zinc blend atomic packing (Fig. 1C) were experimentally determined by several groups to have a dipole moment (*22*–*24*) contributing to the self-assembly of these particles into 1D chains and nanowires (*7*, *24*–*26*). Additionally, DMAET molecules confer some positive charge to the NPs, which we estimate to be 1 to 3*e* as in (*27*). There is also a strong hydrophobic attraction between the NPs, because DMAET has two hydrophobic methyl groups (*28*). We did not deplete the stabilizer layer by precipitating it with methanol (antisolvent), as our group had done previously with thioglycolic acid (*7*). This method maintains the individuality of the NP cores seen in the TEM images (Fig. 1, A and C).

On the basis of these observations and considering the relatively short length of the stabilizers (0.55 nm compared with the NP size of 2 to 5 nm), we conjecture that anisotropic electrostatic interactions arising from both a dipole moment and a small positive charge, combined with directional hydrophobic attraction, are responsible for the formation of the 2D free-floating films. Molecular simulations based on a coarse-grained model with proper parameters determined by semi-empirical quantum mechanics calculations were performed to validate the proposed hypothesis. The origin of the dipole moment in zinc-blend structured NPs is attributed to the truncation of the tetrahedrons (*22*, *24*, *29*). The high-energy apices of the tetrahedron are likely to be replaced with less energetic crystal planes in NPs (*1*, *30*). Some of the four apices may be truncated, and some of them may remain. For the molecular simulations, we start from a model NP with three truncated apices. For a NP of 2.53-nm width and 2.95-nm height (Fig. 3A), semi-empirical PM3 quantum mechanical calculations indicate that the CdTe NP has a dipole moment of 107.74 D when the truncated corners are coated with H_2O and 56.75 D when the truncated corners are coated with sulfhydryl (SH). These values are consistent with reported values of 50 to 100 D (*22*).

A coarse-grained "patchy particle" model proposed previously by Zhang and Glotzer is used to study the self-assembly of NPs with complex shape and anisotropic interactions, here by Monte Carlo (MC) simulations (*31*). Sixty-two beads were rigidly linked together into the shape of a truncated tetrahedron (Fig. 3B). The beads interact with a hard core

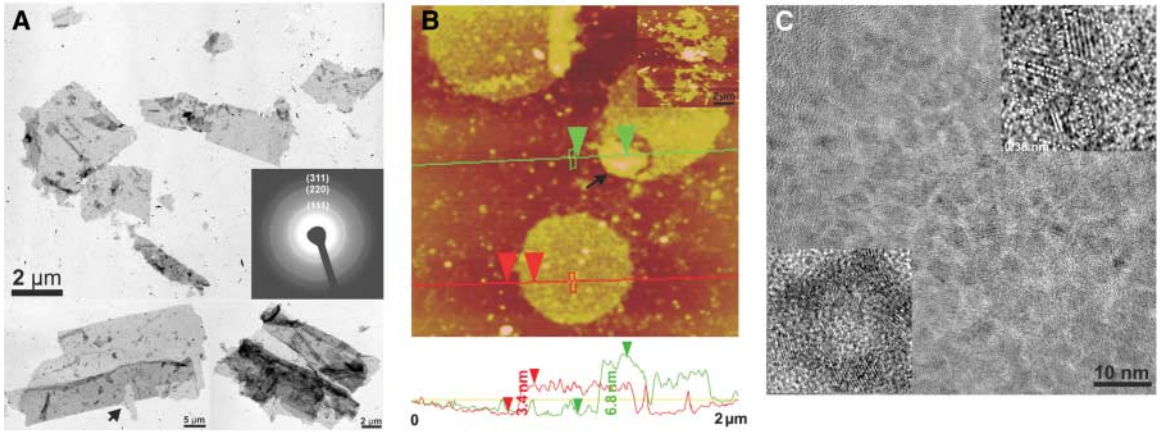

Fig. 1. (**A**) TEM images of free-floating films of CdTe NPs. (Inset) Electron diffraction pattern obtained from the films. (**B**) Tapping-mode AFM and corresponding topography cross sections of the monolayer films on a silica surface. (Inset) Large-scale AFM image of the films. The morphology of the films is the same for hydrophilic and hydrophobic TEM grids, as well as for AFM images obtained on hydrophilic and hydrophobic Si substrates. The drying of the dispersion, which is different on substrates with different wettabilities, is not a factor in the sheet formation. (**C**) High-resolution TEM (HRTEM) images of the monolayer films of CdTe NPs. The inset at top right represents a detailed arrangement of single NPs obtained by HRTEM. Each particle has a distinct cubic crystal structure identified from the spacing between adjacent crystal planes inside the NPs equal to 0.38 nm, which corresponds to (111) surfaces of zinc blend CdTe. Inset at bottom left shows characteristic assembled rings of cubic CdTe NPs with zinc blend cubic crystal structure. The error bars represent the standard deviation.

repulsive interaction to model the excluded volume effect between the NPs. The diameter of each bead is $\sigma = 0.5$ nm. The corresponding NP size is $h = 2.86$ nm and $w = 2.50$ nm, which is close to the size used in the quantum calculation in Fig. 3A. As mentioned previously, the stabilizer length is much smaller than the NP size; therefore, the hydrophobic attraction only exists between the pair faces and is short-ranged and directional. This is modeled by a square-well potential modulated by an angular term (Fig. 3C) (*32*)

$$U_{ij}(r_{ij};\mathbf{Q}_i,\mathbf{Q}_j) = u^{hssw}(r_{ij}) \cdot f(\mathbf{Q}_i,\mathbf{Q}_j) \quad (1)$$

where u^{hssw} is the regular hard sphere square-well potential

$$u^{hssw}(r_{ij}) = \begin{cases} \infty & \text{for } overlap \\ -\xi & \text{for } r_{ij} < 2l + \lambda,\ non-overlap \\ 0 & \text{for } r_{ij} \geq 2l + \lambda,\ non-overlap \end{cases} \quad (2)$$

Here ξ is the depth of the square-well potential related to the strength of the hydrophobic attraction, r_{ij} is the distance between the centers of mass of NP i and j, l is the distance from the mass center of the NP to the tetrahedron face, and λ is the interaction range. The function $f(\mathbf{Q}_i, \mathbf{Q}_j) = 1$ only if NPs i and j are oriented so that the angle between the vector joining their mass centers and the normal vector of the crystal face is less than δ; otherwise, $f(\mathbf{Q}_i, \mathbf{Q}_j) = 0$. The angle δ and interaction range λ in combination determine the directionality of the attraction between the faces of two NPs, which can be estimated by the length ratio of the stabilizer and NP. For example, the stabilizer length is ~0.55 nm and δ is ~18° (Fig. 3A). Thus, we chose $\lambda = 0.55$ nm and $\delta = 18°$ in the MC simulations (Fig. 3C). The electrostatic potential between two NPs U_{ij} is modeled by

$$U_{ij}(r_{ij}) = \frac{q_i q_j}{4\pi\varepsilon_0\varepsilon r_{ij}} e^{-kr_{ij}} C_0^2 + \frac{q_i\mu_j \cos\theta_j + q_j\mu_i \cos\theta_i}{4\pi\varepsilon_0\varepsilon r_{ij}^2} e^{-kr_{ij}} C_0 C_1 + \frac{\mu_i\mu_j}{4\pi\varepsilon_0\varepsilon r_{ij}^3}\left\{\cos\theta_i \cos\theta_j\left[2 + kr_{ij} + (kr_{ij})^2\right] + \sin\theta_i \sin\theta_j \cos(\phi_i - \phi_j)[1 + kr_{ij}]\right\} e^{-kr_{ij}} C_1^2 \quad (3)$$

which was proposed by Phillies for polyelectrolyte colloids and proteins in dilute solution (*33*).

In the above equation, $C_0 = \frac{e^{ka}}{1 + ka}$ and

$$C_1 = \frac{3e^{ka}}{2 + 2ka + (ka)^2 + \varepsilon_0(1 + ka)/\varepsilon} \quad (4)$$

Here q_i and q_j are the net charge carried by NP i and NP j; μ_i and μ_j are dipole moments; r_{ij} is the distance between two NPs; θ_i and θ_j are angles of the dipole vector with respect to the vector connecting the centers of the NPs, where $0 < \theta < \pi$; φ_i and φ_j are dihedral angles describing the relative rotation of dipoles, where $0 < \varphi < 2\pi$; $1/k$ is the Debye screening length, which is set to be 2.5 nm; ε_0 is the permittivity of vacuum; ε is the effective permittivity of the solvent (water); and a is the radius of a NP. The dipole moment is set to be 100 D, as suggested

Table 1. Electrostatic energy of two NPs as a function of relative orientation (separation $r = 0.55$ nm). U_{qq}: charge-charge interaction; $U_{q\mu}$: charge-dipole interaction; $U_{\mu\mu}$: dipole-dipole interaction; U_t: total electrostatic interaction. All energy is in units of kJ/mol. $\Delta\varphi$ is the dihedral angle between the dipole directions of neighboring NPs.

Relative orientation	Bottom-bottom	Bottom-side	Side-side			
			$\Delta\varphi = 0°$	$\Delta\varphi = 60°$	$\Delta\varphi = 120°$	$\Delta\varphi = 180°$
U_{qq}	53.47	53.47	53.47	53.47	53.47	53.47
$U_{q\mu}$	45.63	15.21	−15.21	−15.21	−15.21	−15.21
$U_{\mu\mu}$	12.40	−4.13	5.91	3.64	−0.89	−3.15
U_t	111.50	64.55	44.17	41.90	37.37	34.85

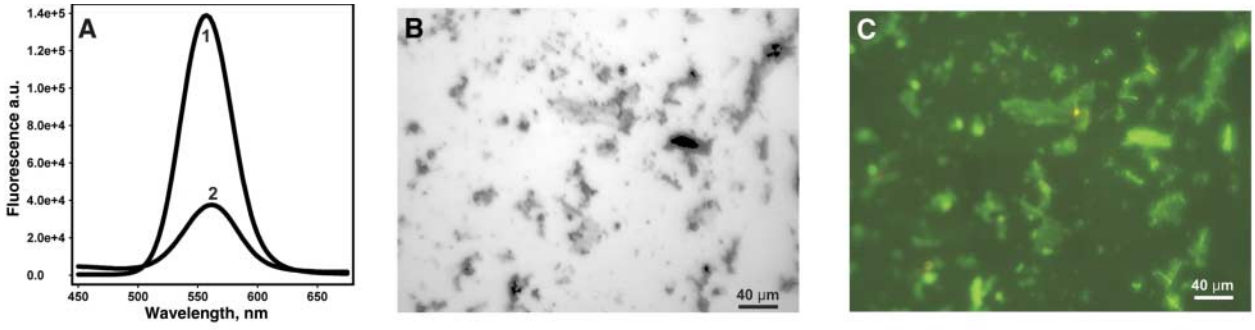

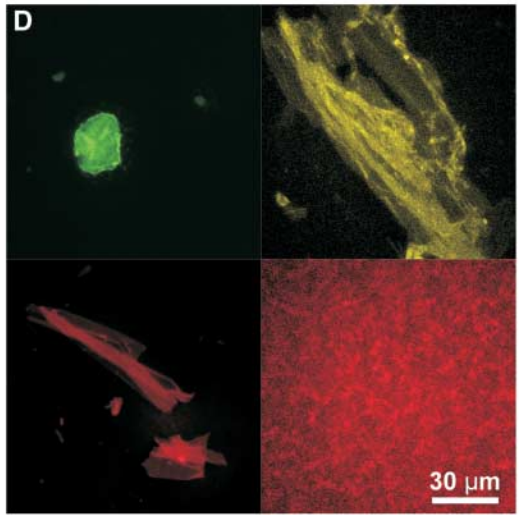

Fig. 2. (**A**) PL spectra of the solution of original CdTe NPs (1) and the dispersion of the free-floating NP films (2). Optical (**B**) and fluorescence (**C**) images of the self-assembled NP sheets. (**D**) Fluorescence images of self-assembled sheets of green-emitting NPs with a diameter of ~2.4 nm (top left), yellow-emitting NPs with a diameter of ~3.6 nm (top right), and red-emitting NPs with a diameter of ~5.0 nm (bottom left). The inset (bottom right) represents an analogous image of red-emitting NPs before self-assembly, demonstrating only disordered aggregation on glass substrates. The optical and fluorescent microscopy images were processed by Leica TCS NT confocal microscopy software. A 488-nm line of a water-cooled Ar-ion laser was used for luminescence excitation.

by our quantum calculations. The net charge q is set to be $+3e$ as determined by experimental measurements (*27*).

MC simulations in the canonical ensemble (constant number of NPs, volume, temperature) are performed in a cubic box with periodic boundary conditions implemented in all three Cartesian directions. A MC step is defined as N (number of NPs) attempts at moving the particles by either translation or rotation. The simulations begin from a disordered state that is obtained by running 3 to 5 million MC steps with attractive energy $\xi = 0.0$ and temperature $T = 25°C$. ξ is then gradually increased from a low value (disordered state) to a high value at which ordered films are formed. We investigated three different systems: $N = 20$ at volume fraction $\phi = 0.13$, $N = 30$ at $\phi = 0.12$, and $N = 60$ at $\phi = 0.13$. Twenty independent runs were performed for the first two systems and four independent runs were performed for the third system. All of them demonstrate that CdTe NPs self-assemble into 2D monolayer films in solution (Fig. 3, D and E). We did not observe sheet formation in simulation in the absence of either the dipole moment, the net positive charge, or the hydrophobic attraction. This point was also exhaustively confirmed experimentally by varying the surface charge, ionic strength, stabilizer length, and the NP material (figs. S3 to S9). For instance, Au NPs with a very small dipole moment do not form the sheets, whereas similar CdSe NPs do. Simulated structures for these cases also match the experimental observations well (figs. S5, S7, and S11).

The simulation results further reveal that the basic units in each 2D monolayer are rings composed of six NPs, in which every bottom-upward NP is adjacent to three corner-upward NPs, and vice versa (Fig. 3E). The ring structures can also be seen in high-resolution TEM images of CdTe NP sheets (Fig. 1C, inset). The large-scale ordering in this system is difficult to discern (Fig. 1C). This is due to variations of NP diameter, geometry, truncations, and stabilizer distribution, which are inevitable for NPs produced in aqueous solutions with a relatively short stabilizer.

It is convenient to introduce the order parameter $S = (\frac{3}{2}\mathbf{S} : \mathbf{S})^{1/2}$ in which $\mathbf{S}$ is the orientational tensor defined by $\mathbf{S} = \langle \boldsymbol{uu} \rangle - \frac{1}{3}\mathbf{e}$, where $\mathbf{u}$ is the unit vector of the dipole moment and $\mathbf{e}$ is the unit tensor, to describe the organization of the NP system, as used for liquid crystals. Ordering in the system should depend on the strength of the specific interactions. Indeed, there is a transition in the order parameter S at $\xi = 58$ to 59.5 kJ/mol as the attraction increases (Fig. 3F), which is similar for different systems (fig. S10). Simulations of larger systems confirmed the stability of the sheets (see supporting online material).

We also evaluate the potential energy between two NPs as a function of relative orientation to elucidate how the locally anisotropic interactions conspire to produce a global symmetry-broken 2D structure. The truncated tetrahedral shape of the NP causes the hydrophobic attraction between them to be anisotropic, i.e., the bottom-bottom, bottom-side, and side-side alignments are favored. The energy of attraction remains the same (square-well interaction) in all of these orientations, whereas the energy of electrostatic interactions does not (Table 1). The combined lowest energy state is the side-side orientation with opposite dipole directions ($\Delta\varphi = 180°$), which we indeed find in the simulations. The energy difference between the lowest energy state (side-side, $\Delta\varphi = 180°$) and the next lowest energy state (side-side, $\Delta\varphi =$

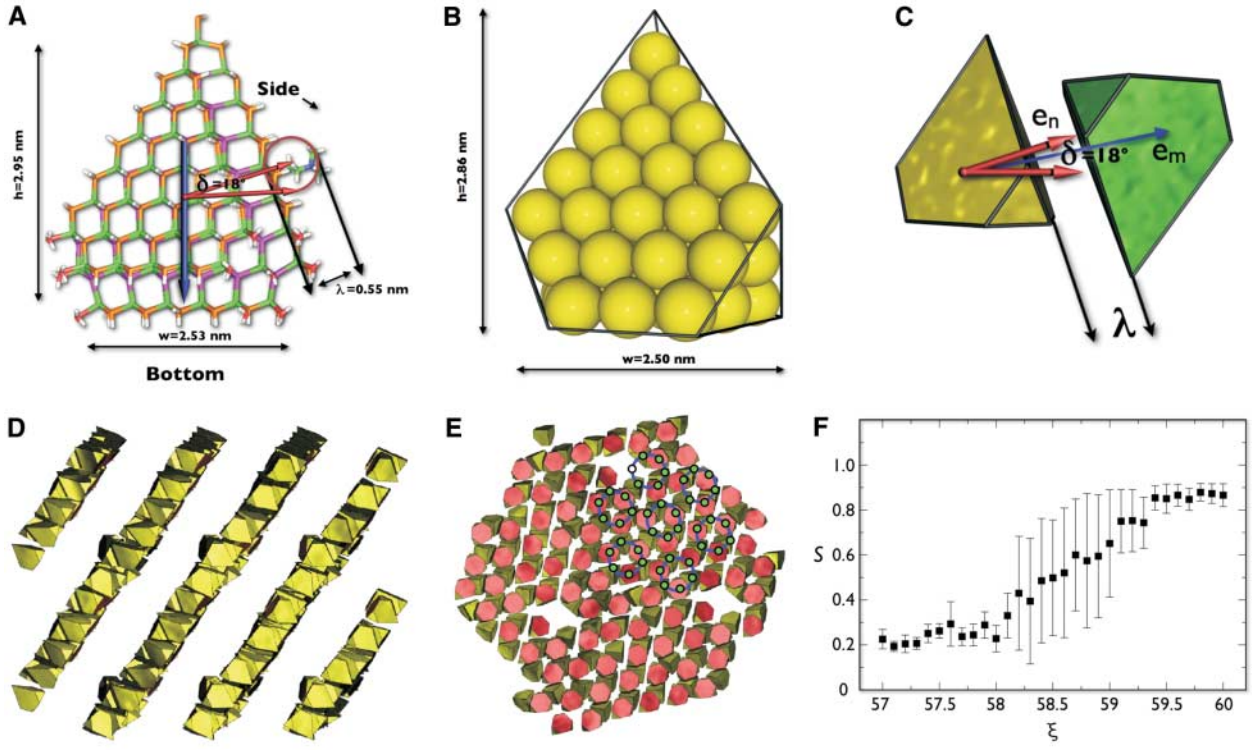

Fig. 3. Computer simulations of self-assembly of CdTe NPs. (**A**) Semi-empirical PM3 quantum calculation of a single CdTe NP by Spartan V4. Colors: Cd (green), Te (purple), S (orange), O (red), and H (white). The surface of the NP is coated by SH groups as a minimal model of the DMAET stabilizers. The stabilizers attached to the truncated corners are either SH or water molecules. The angle δ, which determines the directionality of hydrophobic attraction between faces, is ~18°. The calculated dipole direction is illustrated by the blue arrow. Its negative direction points toward the bottom of the crystal. (**B**) Coarse-grained model of a single NP made from 62 beads of uniform size. (**C**) Schematic illustration of the model for the directional hydrophobic attraction between NPs. $\mathbf{e}_n$ is the normal vector of the faces; $\mathbf{e}_m$ is the vector connecting the mass centers of NPs. Two NPs are attractive only when the angle between $\mathbf{e}_n$ and $\mathbf{e}_m$ is less than $\delta = 18°$. (**D**) Side view of films obtained by mesoscale simulation with $N = 480$ and $\phi = 0.13$. The system size shown here has been doubled for clarity. (**E**) Face view of a single sheet in (D). The basic structure within the sheet is rings composed of six NPs, indicated by dotted circles. (**F**) The dependence of the scalar order parameter, S, as a function of ξ as obtained by an average over four independent runs ($N = 60$ and $\phi = 0.13$). The error bars represent the standard deviation.

120°) is 2.52 kJ/mol, which is comparable with the energy of thermal noise. Table 1 also demonstrates the necessity of a small positive charge in addition to the dipole moment to form sheets. Without net charge the lowest energy state is the bottom-side orientation, preventing the formation of 2D monolayers (fig. S11).

Using the same modeling strategy, one can consider NPs with different numbers of corners truncated. NPs with zero or one truncated corners cannot form 2D monolayers due to the steric constraints between the untruncated corners of adjacent NPs. NPs with two truncated corners form chains instead of monolayers (fig. S12). Although 2D self-assembly was observed only for NPs with three truncated corners, we do not exclude the existence of NPs with other number of truncated corners in the experimentally obtained sheets, including those with four truncated corners, because the net dipole moment inside those NPs can be induced by other adjacent NPs (*24*). The inclusions will show up as defects within the sheet (Fig. 1C). Nevertheless, the arrangement of NPs with three adjacent NPs in a 2D film is the most energetically favorable.

The interactions between NPs in general are complex and diverse, which offers tremendous opportunities for the design of NP assemblies with varying shapes, structures, and functions (*31*, *34*). This study of 2D self-assembly of NPs demonstrates (i) the importance of anisotropy of interparticle interactions at the nanoscale and (ii) methods for the manipulation and prediction of spontaneous NP assemblies. These data also show a surprising resemblance of NPs to self-ordering biological systems, such as S-layer–forming proteins (*4*–*6*). This is particularly important for establishing correlations between protein superstructures and inorganic nanostructures on the basis of their similar sizes.

References and Notes

1. A. P. Alivisatos, *Science* **271**, 933 (1996).
2. C. B. Murray, C. R. Kagan, M. G. Bawendi, *Annu. Rev. Mater. Sci.* **30**, 545 (2000).
3. Z. Y. Tang, N. A. Kotov, *Adv. Mater.* **17**, 951 (2005).
4. U. B. Sleytr, E. M. Egelseer, D. Pum, B. Schuster, in *Nanobiotechnology: Concepts, Applications, and Perspectives*, C. M. Niemeyer, C. A. Mirkin, Eds. (Wiley-VCH, Weinheim, Germany, 2004), pp. 77–92.
5. K. Jagannathan, R. W. Chang, A. Yethiraj, *Biophys. J.* **83**, 1902 (2002).
6. R. Flachmann, W. Kuhlbrandt, *Proc. Natl. Acad. Sci. U.S.A.* **93**, 14966 (1996).
7. Z. Tang, N. A. Kotov, M. Giersig, *Science* **297**, 237 (2002).
8. J. F. Banfield, S. A. Welch, H. Z. Zhang, T. T. Ebert, R. L. Penn, *Science* **289**, 751 (2000).
9. C. Pacholski, A. Kornowski, H. Weller, *Angew. Chem. Int. Ed.* **41**, 1188 (2002).
10. C. B. Murray, C. R. Kagan, M. G. Bawendi, *Science* **270**, 1335 (1995).
11. M. P. Pileni, *J. Phys. Chem. B* **105**, 3358 (2001).
12. A. L. Rogach *et al.*, *Adv. Funct. Mater.* **12**, 653 (2002).
13. C. Burda, X. B. Chen, R. Narayanan, M. A. El Sayed, *Chem. Rev.* **105**, 1025 (2005).
14. E. V. Shevchenko, D. V. Talapin, N. A. Kotov, S. O'Brien, C. B. Murray, *Nature* **439**, 55 (2006).
15. V. L. Colvin, A. N. Goldstein, A. P. Alivisatos, *J. Am. Chem. Soc.* **114**, 5221 (1992).
16. C. P. Collier, R. J. Saykally, J. J. Shiang, S. E. Henrichs, J. R. Heath, *Science* **277**, 1978 (1997).
17. Y. Lin, H. Skaff, T. Emrick, A. D. Dinsmore, T. P. Russell, *Science* **299**, 226 (2003).
18. A. L. Rogach *et al.*, *Ber. Bunsenges. Phys. Chem* **100**, 1772 (1996).
19. N. Gaponik *et al.*, *J. Phys. Chem. B* **106**, 7177 (2002).
20. C. R. Kagan, C. B. Murray, M. Nirmal, M. G. Bawendi, *Phys. Rev. Lett.* **76**, 1517 (1996).
21. S. A. Crooker, J. A. Hollingsworth, S. Tretiak, V. I. Klimov, *Phys. Rev. Lett.* **89**, 186802 (2002).
22. M. Shim, P. Guyot-Sionnest, *J. Chem. Phys.* **111**, 6955 (1999).
23. J. L. Gavartin, A. M. Stoneham, *Philos. Trans. R. Soc. London. A* **361**, 275 (2003).
24. K. S. Cho, D. V. Talapin, W. Gaschler, C. B. Murray, *J. Am. Chem. Soc.* **127**, 7140 (2005).
25. J. Polleux, N. Pinna, M. Antonietti, M. Niederberger, *Adv. Mater.* **16**, 436 (2004).
26. S. G. Thoma, A. Sanchez, P. P. Provencio, B. L. Abrams, J. P. Wilcoxon, *J. Am. Chem. Soc.* **127**, 7611 (2005).
27. A. A. Yaroslavov *et al.*, *J. Am. Chem. Soc.* **127**, 7322 (2005).
28. J. N. Israelachvili, *Intermolecular and Surface Forces: With Applications to Colloidal and Biological Systems* (Academic Press, New York, 1985), p. 296.
29. S. Shanbhag, N. A. Kotov, *J. Phys. Chem. B* **110**, 12211 (2006).
30. Z. L. Wang, *J. Phys. Chem. B* **104**, 1153 (2000).
31. Z. L. Zhang, S. C. Glotzer, *Nano Lett.* **4**, 1407 (2004).
32. M. S. Wertheim, *J. Stat. Phys.* **35**, 19 (1984).
33. G. D. Phillies, *J. Chem. Phys.* **60**, 2721 (1974).
34. Z. L. Zhang, M. A. Horsch, M. H. Lamm, S. C. Glotzer, *Nano Lett.* **3**, 1341 (2003).

35. Experiments were performed by Z.T. and Y.W. Simulations were performed by Z.Z. We thank the NSF (N.A.K.), U.S. Department of Energy (S.C.G.), Air Force Office of Scientific Research (N.A.K.), and Defense Advanced Research Projects Agency (N.A.K.) for the financial support of this research. Seed funding provided by the University of Michigan College of Engineering Nanotechnology Initiative is greatly appreciated. Z.Z. and S.C.G. thank C. Iacovella in the Glotzer group for graphics support. Z.T. and N.A.K. thank Z. L. Wang (Georgia Tech) for preliminary TEM observations.

Supporting Online Material

www.sciencemag.org/cgi/content/full/314/5797/274/DC1
Materials and Methods
Figs. S1 to S12

29 March 2006; accepted 29 August 2006
10.1126/science.1128045

Dynamic Stark Control of Photochemical Processes

Benjamin J. Sussman,[1,2] Dave Townsend,[1] Misha Yu. Ivanov,[1] Albert Stolow[1,2]*

A method is presented for controlling the outcome of photochemical reactions by using the dynamic Stark effect due to a strong, nonresonant infrared field. The application of a precisely timed infrared laser pulse reversibly modifies potential energy barriers during a chemical reaction without inducing any real electronic transitions. Dynamic Stark control (DSC) is experimentally demonstrated for a nonadiabatic photochemical reaction, showing substantial modification of reaction channel probabilities in the dissociation of IBr. The DSC process is nonperturbative and insensitive to laser frequency and affects all polarizable molecules, suggesting broad applicability.

Molecular catalysts increase chemical reaction rates by applying forces that modify potential energy barriers along a reaction coordinate. Because electrical forces underlie all of chemistry, such barrier manipulation is also possible by application of a laser field. The duration of modern ultrafast laser pulses is on the time scale of chemistry itself, and therefore precise control over the form and delay of these pulses offers access to different portions of a potential energy surface as a reaction occurs. DSC is a technique that uses nonresonant infrared laser fields to dynamically alter a potential energy landscape during a photochemical reaction. The application of this field modifies the potential surface via the Stark effect, enhancing or inhibiting a specific reaction channel. Importantly, it does so without inducing any real electronic transitions to other potential surfaces, which can lead to chemical reactions other than the one of interest. DSC will be general because the nonresonant Stark effect is independent of the laser frequency and is applicable to all quantum systems.

The control of chemical reactions by lasers is an area of great interest (*1*–*3*). Quantum control can be viewed as chemistry where light is used as a photonic reagent (*4*). By contrast, we experimentally demonstrated that the nonresonant dynamic Stark effect participates in quantum control by altering reaction barriers, as if it were a photonic catalyst. Because all strong-field approaches tacitly contain the dynamic Stark effect, DSC can be considered as a fundamental element of the quantum control toolbox (*5*). However, by exclusively utilizing the dynamic Stark effect, DSC avoids the ionizing fields that can produce numerous competing processes, such as Coulomb explosion (*6*), enhanced ionization (*7*), and nonadiabatic multielectron ionization (*8*). Perturbative coherent control approaches do not modify potential energy surfaces but rather use interference between two or more real electric dipole transitions (*1*). Strong dipole coupling of states in nonper-

[1]Steacie Institute for Molecular Sciences, National Research Council of Canada, 100 Sussex Drive, Ottawa, Ontario K1A 0R6, Canada. [2]Department of Physics, Queen's University, Kingston, Ontario K7L 3N6, Canada.

*To whom correspondence should be addressed. E-mail: albert.stolow@nrc.ca